Holographic Measurements of the NASA-JPL Deep Space Network Antennas

D. J. Rochblatt
Jet Propulsion 1 .aboratory
California Institute of 'l'ethnology
Pasadena, California 9 I 109
818-354-3516
david.j.rochblatt@jpl.nasa.gov

A *bstract-* Microwave holography, as applied to reflector antennas, is a technique which utilizes the Fourier Transform relation between the complex far-field radiation pattern of an antenna and the complex aperture distribution. Resulting aperture phase and amplitude distribution data arc used to precisely characterize various crucial performance parameters, including panel alignment, subreflector position, antenna aperture illumination, directivity at various frequencies, and gravit y deformation effects. The holography technique provides a methodology for analysis, evaluation, and RF performance improvement of large reflector and beam waveguide antennas. Strong CW signals obtained from geostationary sources arc used as far-field sources. Microwave holography has been one of the most economical technique for increasing the performance of the large DSN antennas in terms of cost to performance ratio. This paper describes the application of the holography technique as applied at the NASA-JPL Deep Space Network (DSN) antennas with an emphasis on the 34-M beamwaveguide (BWG) subnet successfully preparing them for operation at Ka-band (32-GHz). A table summarizing the holography historical data is also included. Recent results in which we aligned the panels ofjht'three 34-M BWG antennas (DSS-24, DSS-25 and 1) SS-26) to an rms surface precision of 0,25 mm is described. The precision of these antennas (diameter/rms) is 1.36x105 and their gain limit is at 95 GHz.

TABLE OF CONTENTS

1. INTRODUCTION

The NASA-JPL Deep Space Network (DSN) of large reflector antennas is subject to continuous demands for improves' signal reception sensitivity, as well as increased transmitting power, dynamic range, navigational accuracy, and frequency stability. in addition, once-in-a-lifetime science opportun it ies have increased requirements of the DSN performance reliability, while needs for reduction of operational costs and increased automation have created more demands for the development of user friendly instruments. The increase of the antenna operational frequencies to X-band (8.45 GHz) and Ka-band (32 GHz), coupled with higher performance requirements by new missions like the Cassini radio science experiment (e.g. gravity wave detection) created a demand to derive high precision (and high resolution where applicable) antenna gain, pointing, panel and subreflector alignment, and antenna stability. As an example, for an adequate performance of an antenna at a given frequency it is required that the reflector surface (rms) accuracy be $\lambda/20$ (0.46 mm at Ka-band) and that the pointing accuracy (rms) be approximately $\lambda/(10*D)$, or a tenth of the beamwidth (1.6 mdeg for a 34 M antenna at Ka-band).

The Microwave Antenna Holography System (MAHST) was developed at JPL in the late 1980's under the Advanced System Program. Under the a new reorganization, similar R&D developments are now managed by the Telecommunications and Mission Operations (TMO) Technology [development Program. The success of the MAHST[1] has inspired other precision measurement techniques to be developed to meet the requirements of the large DSN antennas at 32 GHz [2], [3].

2. MICROWAVE ANTENNA HOLOGRAPHY

I holography, "total recording," acquires phase and amplitude raster-scan (most popular, although other scans geometry are possible and could be advantageous under certain conditions) patterns of the antenna angular response. I holographic metrology is based on interferometrically connecting a reference antenna to the large test antenna and digital ly recording the test antenna amplitude and phase response. This is done by continuously scanning the test antenna against a signal source from a Geosynchronous satellite, following a two-dimensional grid. The angular extent of the response that must be acquired is inversely proportional to the size of the desired resolution cell in the processed holographic maps. An inverse fast Fourier transform (FFT) algorithm is then used to obtain the desired information, consisting of the test antenna aperture amplitude and phase response [1],[4],[5],[6]. From the aperture phase response, the surface error map is calculated and the amplitude response is directly displayed. It is the information in the surface

error map that is used to calculate the adjustments of the individual panels in an overall main reflector best-fit reference frame. The amplitude map provides valuable information about the energy distribution in the antenna aperture .

The microwave antenna holography system (MA}{ ST) implementation for the DSN satisfies the requirements for fast (45 rein) "health check" measurement utilizing low-resolution medium-precision images to determine the antenna status. It also provides high-resolution high-precision images measured over a 12-h period for the 70 M antenna and for a 6 h period for the 34-M antenna to provide reflector panel setting adjustments. The systcm allows for technological growth, in order to provide a major tool for future studies of understanding factors such as thermal, wind, reflector panel manufacturing and setting precision, beam pointing, focus, gain, phase stability, mechanical hysteresis, weather, paint, and aging.

3. MAHST DESIGN

In the earlier design stages we analyzed and compared two major approaches for the system architecture: wide bandwidth versus narrow bandwidth receiver. To facilitate the examination of the two approaches wc developed simulation algorithms.

The parameters critical for the quality of the images derived from holographic measurements are signal-to-noise ratio, maximum scan angle, instrumentation dynamic range, related approximations which may bc included due to different sampling techniques, and overall system accuracy, A detailed mathematical derivation of the related equations can be found in [6] and [7]. In general, to derive the standard deviation in the final holographic map from simulation, a far-field pattern of the perfect reflector antenna is first computed. By superimposing the contribution of the measurement system noise on the far-field patterns, a simulation tool is developed [8]. By processing the new far-field data and displaying the images, one obtains the standard deviation in processed holographic maps. For the simulations case study the NASA 64-M antenna with -13 dB amplitude taper was used (the three 64-M antennas were later extended to 70-M dual shape cassegrain systems).

the accuracy in the final maps can be formulated from the simulation results to be:

$$\sigma \cong .082 \frac{\lambda D}{\delta \, SNR} \tag{1}$$

where:

σ:	standard deviation (accuracy) in recovering the mean position of a resolution cell
λ:	wavelength
D:	reflector diameter
δ	spatial resolution in the aperture plane

SNR	beam peak voltage SNR in the test (antenna) channel.

Equation (1) agrees well with the analytical expressions derived in [6] and [7]. Here, the constant 0.082 was empirically determined based on the simulation results which agree well with the analytical ly derived constant of $1/4\pi$. As will be shown in the simulation results, the accuracy across holographic maps varies with the aperture amplitude taper illumination. Results are better at the center of the dish and gradual ly become worse toward the edge of the dish. For a uniformly illuminated dish, accuracy stays relatively constant through most of the dish and quickly becomes worse just at the edge where the illumination falls off rapidly.

Aperture simulation models are used because of their simplicity and usefulness. They allow an examination of the interrelations between the standard deviation in the holographic maps and a known feature on the reflector surface. In these models, aperture and phase distribution are typically defined and then far-field data are constructed. In general an integration or FFT scheme may be used to obtain the fir-field data. } lowever, for certain special aperture distributions, such as those which are circularly symmetric, *closed-form* expressions can be used [9]. This allows an accurate and efficient far-field pattern generation. The steps of this aperture model follow.

The geometry of a circular aperture with different annular regions is shown in Figure 1.
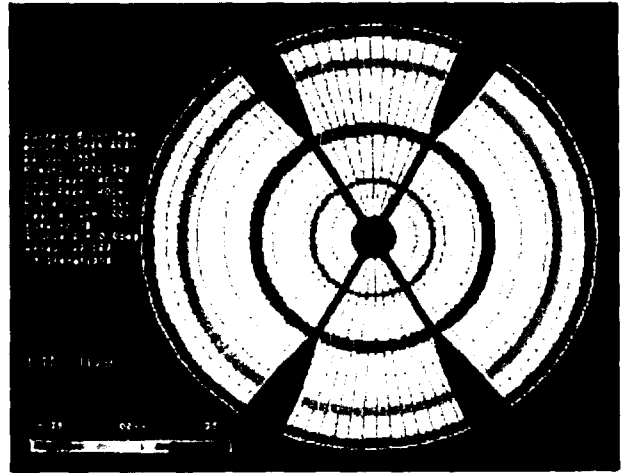

Figure 1. Geometry of Simulated Reflector Distortions

where the regions are designated by red and blue color. In the figure the green color represents a perfect dish surface relative to the best fit paraboloid, while it is assumed that the red and blue colors which represent regions which are deformed by a constant value of+/- 0.2 mm respectively, causing a constant phase irregularities (please note that the scale in Figure 1 is +/- 0.35 mm). We father assume that the amplitude and phase distributions across the aperture are circularly symmetric closed form functions. These assumptions allow one to express the far-field integral in terms of a one-dimensional integral.

Furthermore, for an appropriately chosen amplitude distribution, this integral can be integrated in a closed form. This closed-form expression can be used to construct the far field.
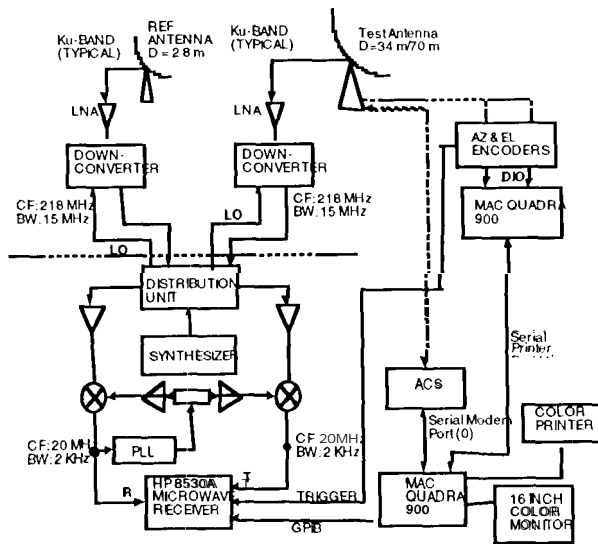
Once the far-field amplitude and phase data are generated, they can then be used in the error simulation algorithm by appropriately injecting noise in a manner that simulates the exact architecture of the holographic measurement system and its front-end noise.

A narrow-bandwidth system was designed with a wide dynamic range and linear response. The system makes use of geostationary satellite beacon signals (nearly CW) available on nearly all satellites at Ku-band (1 1.45 GHz), X-band (7.7 GHz), S-band (2.2 GHz) and perhaps on other bands in the future. The IF section of a network analyzer HP 8530A dB, phase-locked to an external phase-locked loop, provided the heart of the MAHST architecture Figure 2.

Figure 2. MAHST Block Diagram

Rather than cross-correlating the two channels, which is a multiplicative operation, the H P 8530A uses synchronous detectors for the 1 and Q components of the test and reference channels, with a 19 b resolution A/D converter, to form the ratio of test-to-reference channel which provide the real and imaginary components of the complex far-field function. Amplitude variations in the satellite signal cancel out in the division operation. This feature is especially critical since no control over the satellite signal power level is reasonable. Also, since the reference channel SNR in this scheme can easily be 40 dB or better, it can be safely used in the denominator (this would not be desirable for weak reference signals).

The MAHST provides a linear dynamic range of better than 96 dB down to integration periods of 0.2 msec. With satellite beacon EIRP of about 11 dBW, a beam peak SNR of 73 dB is achieved on the 70-M antenna at

Ku-band (12 GHz) with 0.1 s integration period using a simple room-temperature FET (100 K) amplifier, while a 2.8 m reference dish provides 40-45 dB in SNR using a room-temperature (100 K) FET.

For a multiplier integrator as well as a divider integrator receiver architecture, the effective signal SN R_E can be expressed:

$$SNR_E = \left[\sqrt{\frac{1}{SNR_T^2} + \frac{1}{SNR_R^2} + \frac{1}{SNR_T^2 SNR_R^2}} \right] \quad (2)$$

where SNR_T and SNR_R are the test channel and reference channel SNR 's, respectively. The generality of this formulation makes it useful for many different receiver architectures.

From equation (2), it is apparent that the effective SNR_E is dominated by the weaker of the two channels. What this means is that the beam peak SNR_T (of 73 dB) is not realized, and the first few data points on beam peak and a few sidelobes have an effective SNR_E (of approximately 45 dB) of the reference SN R_R. Once the test channel SNR_T drops below the reference antenna SN R_R (45 dB), it doesn't "hurt" the effective SNR_E, which, from that point, follows the same function as the test antenna beam patterns (SNR_T). This is acceptable since very few data points are affected (approximately 0.5%), and since by the nature of the data processing through the Fourier transform operation, all the data points in the far field contribute t each and every point in the aperture, as is shown in the simulations below.

To relate the standard deviation in the final holographic maps to the measurement SNR and receiver architecture, a simulation algorithm has been written in which each channel of the receiver 1 and Q components of both the test and reference channels has added independent noise processing components n, for which the 1 σ in the random Gaussian function is:

$$1\sigma_T = \frac{amp_T (\text{max})}{SNR_T} \quad (3)$$

amp_T (max): beam peak amplitude in the test channel

$$1\sigma_R = \frac{amp_R (\text{max})}{SNR_R} \quad (4)$$

amp_R (max): beam peak amplitude in reference channel.

for the test and reference signals, respectively. The function of the IF section of a divider integrator receiver (i.e., HP 8530A) has been simulated to provide the resultant measured complex quantity including noise:

$$complex \ field = \frac{amp_T (\theta_i) e^{j\phi_{ii}} + n_{R_i}^T + jn_{Ii}^T}{amp_R e^{j0} + n_{R_i}^R + jn_{Ii}^R} \quad (5)$$

$\text{amp}_T(\theta_i)$: test antenna far-field amplitude voltage at the sampled data position θ_i.

ϕ_{Ti}: test antenna far-field phase at the sampled data position i.

$n^T_{R_i}$: noise component in the complex real part of the digitized data sample i in the test channel.

n^T_{Ii}: noise component in the complex imaginary part of the digitized data sample i in the test channel

$\text{amp}_R e^{j0}$: reference channel far-field constant amplitude and phase value.

$n^R_{R_i} + n^R_{Ii}$: noise components in the reference channel real and imaginary parts of the digitized sample data.

This simulation examined, the effect of the SNR in the reference and test antennas on measurement accuracy.

In the simulation, four rings of panels have been intentionally displaced by 0.2 mm (A/130 at 11.45 GHz). Three rings were displaced positively and one was displaced negatively. The width of the three outmost rings is 2.0 m (76 λ) and the innermost rings is 1.0 m wide. The rms surface error of this model (Figure 1) is 0.11 mm. The far field for the above reflector geometry was generated and then contaminated with noise due to the front end, according to the model represented by (5). The far-field data were then processed to display the recovered surface error maps and compute the surface rms errors.

In Figure 1, the far field was processed with no noise
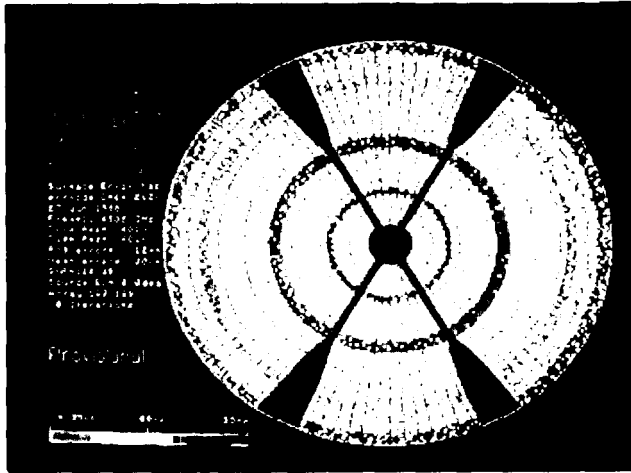
Figure 3. Simulation II.

added to it. This simulated an SNR of more than 90 d B. The computer computational errors are at a level of about λ /5000 (1 1.45 GHz). By subtracting (map differencing) this model from subsequent simulations, a measure comparable to measurement system standard deviation is obtained. Simulation II, (Figure 3) models the conditions where the test antenna SNR on beam peak in

0.1 s integration period is 73 dB and the reference antenna constant SNR is 40 dB. The recovered rms of the test antenna surface is 0.12 mm and the measurement system standard deviation is 0.07 mm (λ /370 at 11.45 GHz).

Simulation III, (Figure 4) simulates conditions in which the test antenna beam peak SNR in 0.1 s integration period is 68 dB and the reference antenna SN R is 40 d B. The recovered surface rms is 0.16 mm with a standard deviation of 0.13 mm.
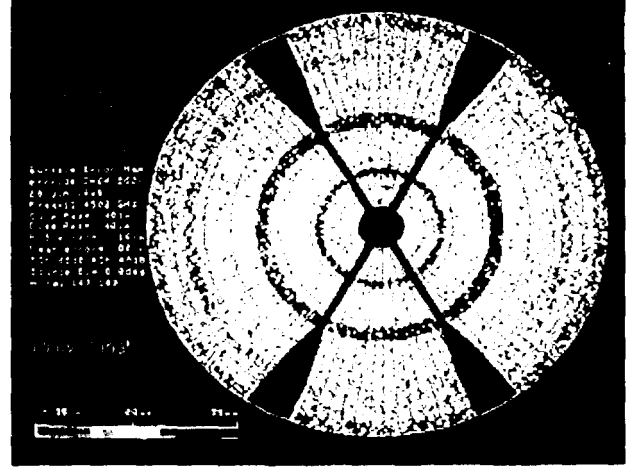
Figure 4. Simulation III.

From simulation IV, (Figure 5) it is clear that the recovery of the dish surface error is very poor when the SNR drops to 58 dB. The necessity of high-beam peak SNR for high-resolution, high-precision holographic measurement is clearly demonstrated [8].
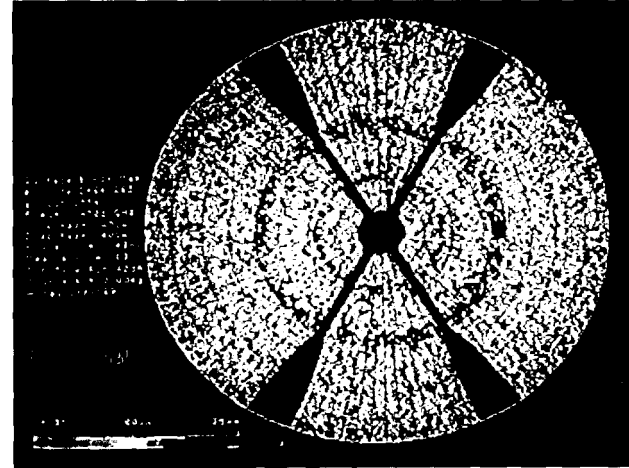
Figure 5. Simulation IV.

4. MATHEMATICAL ALGORITHMS

The mathematical relationship between an antenna far-field radiation pattern (7) and the antenna surface-induced current distribution (J) is given by

$$\vec{T}(u,v) = \iint_S \tilde{J}(x',y') \exp(jkz') * [\exp[-jkz'(1-\cos\theta)]]$$

$$\bullet \exp[jk(ux' + vy')]dx'\,dy' \quad (6)$$

where

$z'(x', y')$:   defines the surface S

u, v: direction cosine space

θ: observation angle

For a small angular extent of the far-field pattern, this expression reduces to

$$\vec{T}(u,v) = \iint_S \tilde{J}(x',y') \exp(jkz') \bullet \exp[jk(ux' + vy')]\,dx'\,dy' \quad (7)$$

Equation (7) is an exact Fourier Transform of the induced surface current. To derive the residual surface error, geometrical optics ray tracing is used to relate the normal error, &, to the axial error and phase in a main reflector paraboloid geometry (Figure 6):
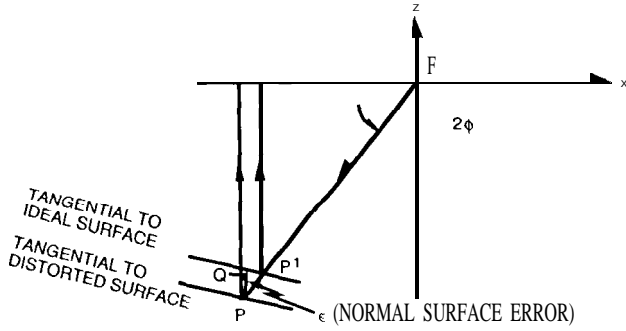
Figure 6. Surface Distortion Geometry.

$$1/2\ \Delta PL = 1/2[P'P + PQ] = 1/2\left[\frac{\varepsilon}{\cos\varphi} + \frac{\varepsilon\ \cos 2\varphi}{\cos\varphi}\right] \quad (8)$$

$$= \varepsilon\ \cos\varphi$$

$$\text{Phase } (APL) = \frac{4\pi}{\lambda}\varepsilon\ \cos\varphi \quad (9)$$

aod

$$\cos\varphi = \frac{1}{\sqrt{1 + \dfrac{X^2 + Y^2}{4F^2}}} \quad (10)$$

F: Focal length.

Allowing for the removal of a constant phase term and substituting (9) into (7) yields:

$$T(u,v) = \exp(-j2kF)\iint_s |\tilde{J}(x',y')|\ ''\ \exp\left(j4\pi\frac{\varepsilon}{\lambda}\cos\varphi\right)$$

$$\bullet[\exp[jk(ux' + vy')]dx'\,dy' \quad (11)$$

For the processing of sampled data, the associated Discrete Fourier Transform (DFT) is utilized:

$$T(p\Delta u, q\Delta v) = sx\ sy \sum_{n=-N1/2}^{N1/2} I\sum_{m=-N2/2}^{N2/2-1} J(nsx, msy)\bullet\exp\left[j2\pi\left(\frac{np}{N1} + \frac{mq}{N2}\right)\right] \quad (12)$$

where

$N1 \times N2$: is the measured data array size

sx, sy: sampling intervals on the aperture coordinates

n, m, p, q: integers indexing the discrete samples

$\Delta u, \Delta V$: sampling interval in the U, V far-field space

Since the magnitude of the far-field pattern is essentially bounded, the Fast Fourier Transform (FFT) is usually used for computation, and symbolized here by (F). Solving for the residual normal surface error and substituting (10), we obtain:

$$\varepsilon(x, y) = \frac{\lambda}{4\pi}\sqrt{1 + \frac{x^2 + y^2}{4F^2}}\ Phase\ [\exp(j2kF)F^{-1}[T(u, v)]] \quad (13)$$

The spatial resolution in the final holographic maps is defined [1], [10]:

$$\delta = \frac{D}{kN} \quad (14)$$

where:

D: main reflector diameter

N: the square root of the total number of data points

k: sampling factor, usually $0.5 < k < 1.0$

The resulting aperture function needs to be corrected for modulo-2π phase errors, and a global least-square fit perform on the data to the "best-fit" paraboloid. This process also allows for the correction of antenna pointing errors introduced during the measurement. The "best-fit" paraboloid is found by minimizing S, the sum squares of the residual path length changes:

$$S \sum_{n=1}^{N2} \Gamma(\Delta PL_i)^2 A_i \quad (15)$$

where:

Γ: support domain constraints masking operator

APL_i: path length change

A_i: amplitude weighting factor

with respect to 6 degrees-of-freedom of the reflector motion; three vertex translations, two rotations, and a focal length change. The six partial differential equations, which are solved simultaneously, are of the form:

$$\frac{\partial S}{\partial Par} = 2 \sum_{i=1}^{N^2} \Gamma \frac{\partial \Delta PL_i}{\partial Par} \, APLiAi = 0 \qquad (16)$$

where:

Par: One parameter of the 6 degrees-of-freedom.

It is correct to apply the best-fit paraboloid algorithm to either the conventional cassegrain paraboloid-hyperboloid or dual-shaped reflector systems even though the latter do not use a paraboloid as the main reflector. Either design is a planewave-to-point source transformer, differing only in the field intensity distribution. The resultant aperture function at the end of this process is referred to as "Effective Map" since it includes all phase effects that are contributing to the antenna performance. These effects include the subreflector scattered (frequency-dependent) feed phase function. Removal of the feed phase function and subreflector support structure diffraction effects results in a frequency independent map, which is referred to below as the "Mechanical Map."

Panel setting information is derived by sorting together all the data points within each panel and performing a least squares fit. The algorithms allow for *one* translation and two rotations, $S\,{}^{'}$, a^k, β^k, hence a rigid body motion. For each panel and its associated *n* data points we solve for the motion parameters via equation (17) (Figure. 7):
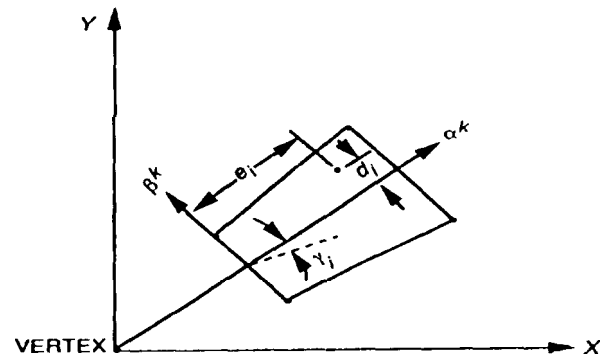
Figure 7: Reflector Panel Geometry

$$\begin{vmatrix} \sum\limits_{i=1}^{n} \cos^2(y_i) & \sum\limits_{i=1}^{n} d_i * \cos^2(\gamma_i) & -\sum\limits_{i=1}^{n} e_i * \cos(y_i) \\ \sum\limits_{i=1}^{n} d_i * \cos^2(\gamma_i) & \sum\limits_{i=1}^{n} d_i^2 * \cos^2(\gamma_i) & -\sum\limits_{i=1}^{n} e_i * d_i * \cos(\gamma_i) \\ -\sum\limits_{i=1}^{n} e_i * \cos(\gamma_i) & -\sum\limits_{i=1}^{n} d_i * e_i * \cos(\gamma_i) & \sum\limits_{i=1}^{n} e_i^2 \end{vmatrix} \begin{bmatrix} S^k \\ \alpha^k \\ \beta^k \end{bmatrix} = \begin{vmatrix} -\sum\limits_{i=1}^{n} \varepsilon_i * \cos(\gamma_i) \\ \sum\limits_{i=1}^{n} \varepsilon_i * d_i * \cos^2(\gamma_i) \\ \sum\limits_{i=1}^{n} \varepsilon_i * e_i * \cos(\gamma_i) \end{vmatrix} \qquad (17)$$

This mathematical process also increases the accuracy in determining the screw adjustment correction by a factor of $\sqrt{n}$.

5. 34-M BWG R&D ANTENNA

In August 1990, holographic measurements from the cassegrain f1 focus of the new DSS 13 BWG antenna were made (Figure 8). Strong CW signals from geostationary satellite beacons were used as far-field sources. Three different geostationary satellites were scanned, producing high- and medium-resolution data sets at elevation angles of 46.5 degrees, 37 degrees, and 12.7 degrees. The measurements obtained provided the necessary subreflector position information, panel setting information, a look at the adjusted surface of the antenna, and information about the gravity performance of the structure at a low elevation angle. The holographic antenna measurements used satellite signal and ephemeris information supplied by

Figure 8: The DSS-13 BWG Antenna in August 1990.

several commercial companies for GTE (GSTAR WI 03), GE (SatCom K1), and CornSat (Intelsat V).

Functionally, the outer 0.6 meter of the DSS - 13 antenna is a noise shield. The rms error obtained from analysis of the central 32 meters of the antenna is therefore more representative of the actual surface than the rms obtained from examination of the full 34-M dish. Therefore we will present here only the rms values for the central 32 meters of the antenna. The precision in the derived surface error maps is 0.05 mm (50 micron). In general, the indicated rms increases as the lateral resolution of the measurement increases (equations 1 and 14). This is an expected result as there is less area averaging occurring as the resolution increases. The asymptotic or infinite resolution rms can be estimated by analyzing the scan data at varying resolutions.
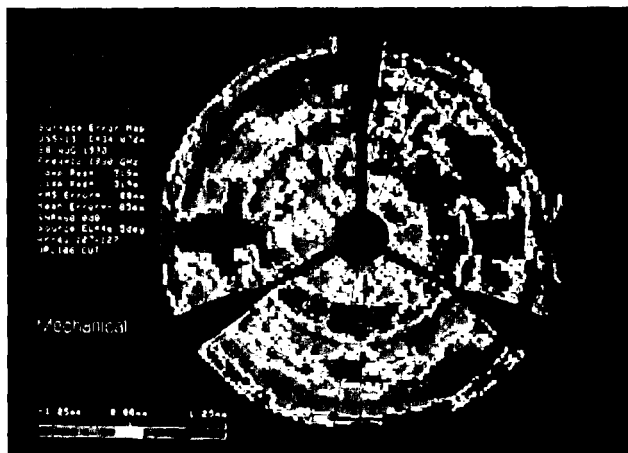
Figure 9: DSS-1 3 After the Initial Theodolite Setting

It is estimated that the rms error found by holography high-resolution (0.32 meter) scans is 8% below the infinite resolution rms. Figure 9 shows the surface error map of the central 32 meters of the DSS 13 antenna surface as found on August 28, 1990 at 46.5 degrees elevation. The main reflector surface normal rms error was found to be 0.88 mm (0.77 mm axial) at a resolution of 0.32 meters.

This measurement supplied the data required for verifying the subreflector position, analyzing the antenna surface, and providing the panel setting information. The surface images derived from the aperture plane phase represent the antenna surface deviations from ideal in the surface normal direction. In the images, the subreflector, the tripod and its shadows, and the bypass beam waveguide are intentionally masked out. The remaining surface is overlaid with an outline of each reflecting panel. The surface error information is shown in pseudo color, with red and blue indicating the high and low deviations, respectively. The panel setting information derived from this scan was applied to the 1716 surface panel adjusting screws for this antenna. As a scheduling expedient, it was decided to adjust the surface panels by turning the adjusting screws to the nearest I/8 of a turn (O. 16 mm). Screws requiring adjustment of less than ± 1/8 or a turn were not touched.

Figure 10 was derived on September 7, 1990 after the first application of holography panel resetting. The image reveals that the panels in the outer two rings are over-bent. The rms surface error achieved by holography-based rigid body panel adjustment is 0.43 mm surface normal at a resolution of 0.32 meters (Table 1). The post-holography surface provides a performance improvement (G/T) of about 0.32 dB at X-band (8.45 GHz), and 4.6 dB at Ka-band (32 GHz). The measured antenna efficiency at 46 degrees elevation, after the holography panel setting was 52.3% at Ka-band (32 GHz) and 75.4% at X-band (8.45 Ghz).
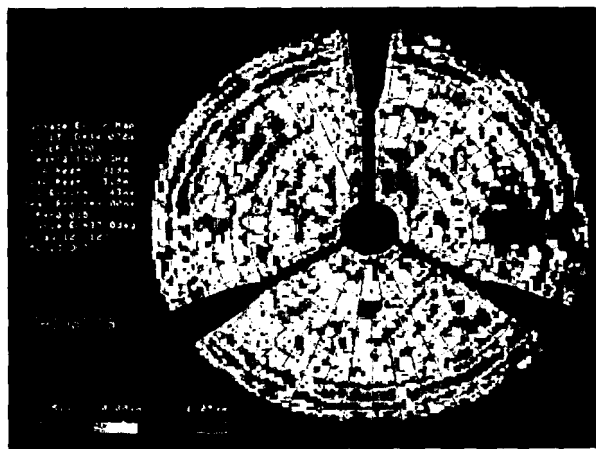

Figure 10: DSS-13 After First Application of Holography

Gravity Performance of the B WG antennas:

The surface error map shown in Figure 11. was derived from medium-resolution, 0.80 meter holography measurements made on September 18, 1990 at an elevation angle of 12.7 degrees. The surface normal rms error at this low elevation angle and resolution is 0.50 mm. The measured antenna efficiency at 12.7 degrees elevation was 39.4% at Ka-band and 74.0% at X-band.
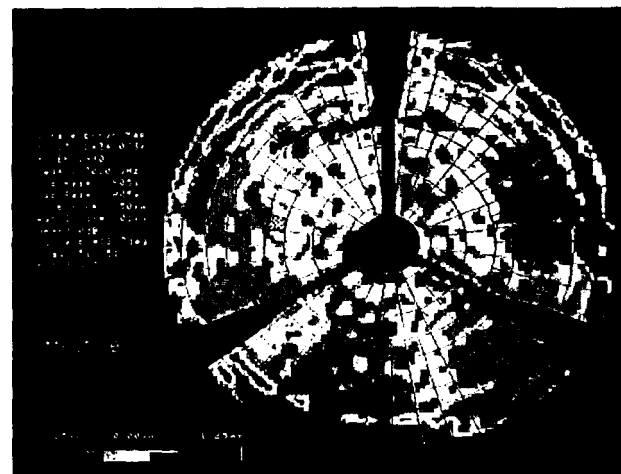

Figure 11:1 Holographic Imaging at 12.7 degrees Elevation

7

The asymmetry revealed in this holographic low elevation map is attributed to the bcamwaveguide (BWG) bypass Figure 8. Expectations were that removing the bypass would eliminate the asymmetrical gravity distortion and
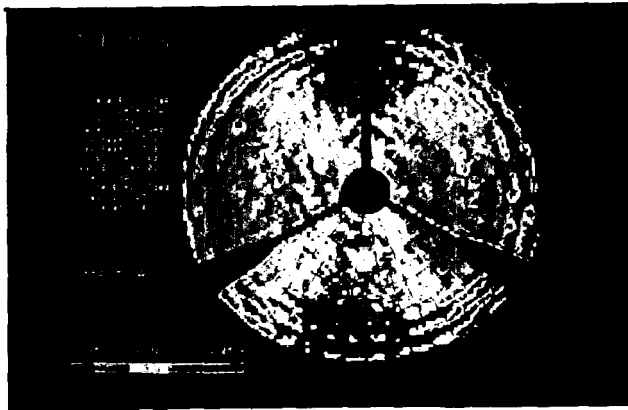

Figure 12: *1)* S-13 Imaging after Removing the Bypass

improve the *32 GHz* gravity performance of the antenna. After the removal of the bypass BWG, and replacement with four panels, the measured gravity distortion function was indeed symmetrical Figure 12. However, the performance of the antenna as a function of elevation angle did not improve. Actually, the antenna gravity performance roll-off after the bypass removal was 2.3 dB between 46 and 12.7 degrees elevations at Ka-band while with the bypass in place it was only 1.2 dB. From this test (and combined with structural analysis by Roy Levy) it was clear that the bypass structure although causing asymmetrical gravity response, was adding significant stiffness to the antenna structure highly desirable for improved Ka-band performance. The lessons learned from this test were applied to all future NASA-JPL-DSN 34-M BWG antennas, building them stiffer thereby achieving gravity deformation loss of only 1.0 dB at Ka-band (the new 34-M BWG antennas have a quadripod support for the subreflector). A deformable flat plate is now under design and implemented to further reduce the performance degradation due to gravity to 0.25 dB.

Panel Unbending

During the planning stages of the *ENS-13* Beam waveguide (BWG) antenna project in 1988 it was decided to compromise and manufacture the main reflector panels by utilizing the existing DSS-15 , 34-M High Efficiency (HEF) antenna panel molds. The differences in the shape of the panels were thought to be minor, and it was believed that they would not significantly affect the required performance of the new research and development antenna. After the initial holographic imaging of DSS-13 in August 1990, and after the derivation of the "predicted mechanical surface error map," (not shown here) and further confirmed after the initial holography derived panel setting, it was discovered that the panels in rings 8 and 9 were systematically overbent (Figure 1 O). It was also predicted that, based on the rigid body panel setting algorithm, the best achievable rms surface error of DSS-13 would be 0.36 mm. Figure 13. shows the mechanical

surface error map that was obtained (January 1992) from the holographic measurements made on the DSS-13 after the removal of the BWG bypass and the application of a
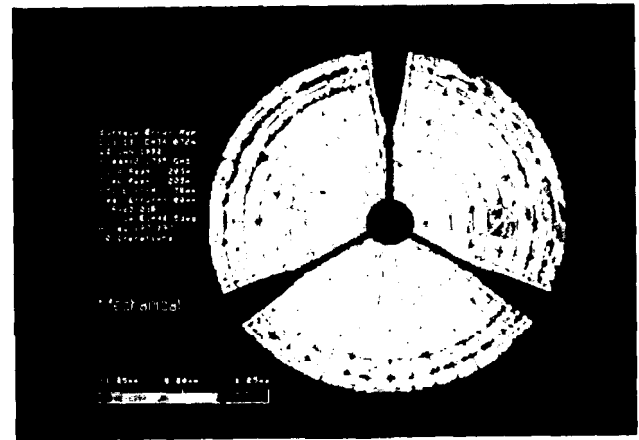

Figure 13: DSS-13 Second Application of Holography

second holographic panel setting to tbe antenna. The normal rms surface error achieved was 0.38 mm which agrees well with the 1990 predicted (best achievable by panel setting) surface of 0.36 mm. This reduction in rms contributed an additional 0.26 dB performance increase (G/T) at Ka-band (Table 1). The deformed panels in rings 8 and 9 are clearly noticeable in figures 10 and 13. Figures 14 and 15 show the holographically derived surface errors for rings 8 and 9, respectively, overlaid on the predicted mechanical surface errors for these panels.
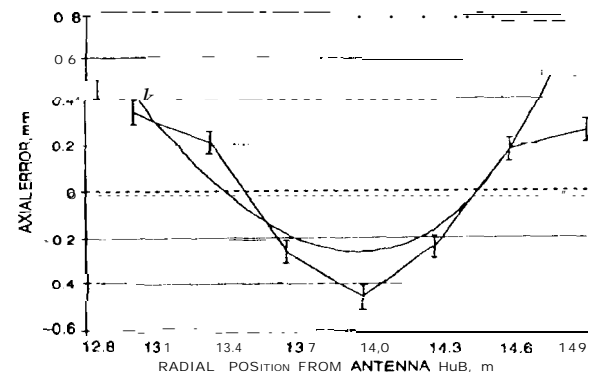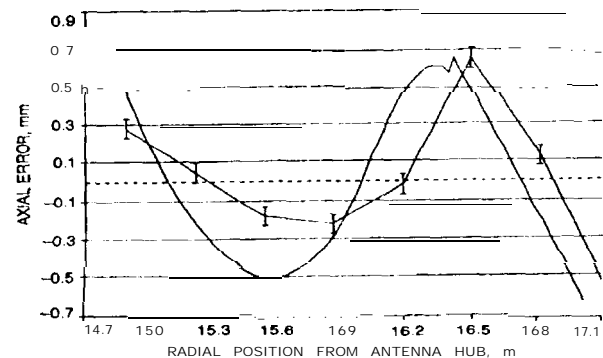

Figure 14: Mechanical Error in Panel Ring 8

Figure 15: Mechanical Error in Panel Ring 9

In these plots the holography data sampled 7 data points across rings *8* and 9, while the solid line is the actual differences between the panel molds. These plots show good agreement between the manufacturing contour and the holography measurements. The normal rms surface error of the inner 7 rings (inner 26 meter) of DSS- 13 is 0.28 mm and the rms in the last two rings of panels is *0.60* mm (Figure 13). The potential increase of performance at Ka-band by achieving 0.28 mm rms for the entire dish is 0.5 dB. Since the cost of replacing the panels in rings 8 and 9 to the correct shape was estimated at over $300K, it was decided to support the proposal to unbend the panels in rings 8 and 9 by utilizing the microwave holography imaging technique. Figures 16 and 17 are the far-field pattern amplitude and phase respectively for this measurement.
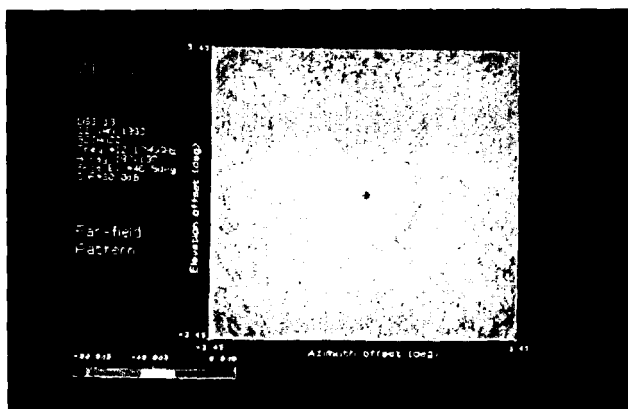
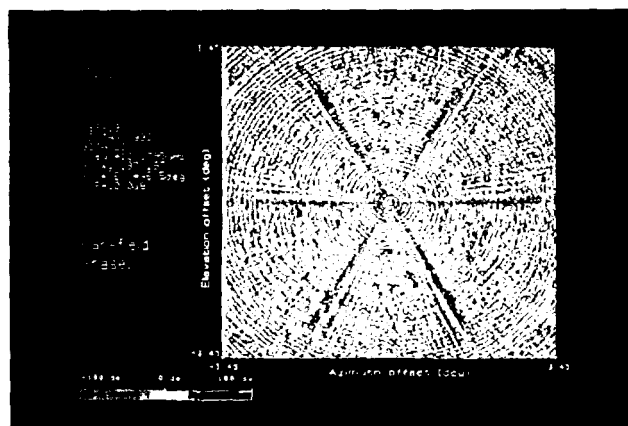Figure 16: Far-Field Amplitude Pattern

Figure 17: Far-Field Phase Pattern

Figure 18 is the aperture amplitude map. The panel gap are clearly visible in these super high resolution images (Figures 13 and 18) as well as the bent in the center of ring 8 where the central screw is positioned.

During the early part of February 1994, three high-resolution holographic measurements were made at DSS-13. The average time per measurement period was 6 hours 45 rein, and the average data processing time (on-site) was 6 hours. The first holographic measurement derived the panel unbending information, the second holographic measurement derived panel setting

information, and the last measurement derived the current state of DSS- 13. All panel setting and panel unbending were rounded to the nearest ±1/8 (+0.16 mm) of a screw turn (a dial indicator was not used). Figure 19 is a high-resolution (34.3 cm) mechanical surface error of DSS - 13, derived from the (last) February 10, 1994 measurement. The achieved normal rms surface error is 0.31 mm, correspond ng to additional 0.32 dB performance improvement at Ka-band (Table 1). A systematic feature which appears in the image of the Figure 19 is the overbend in the corners of panels in rings 8 and 9. An inspection of the DSS - 13 surface confirmed this observation. The adjusting screws, which are positioned approximately 5 inches from the actual comer of the panels do not provide a mechanism for unbending the comers.
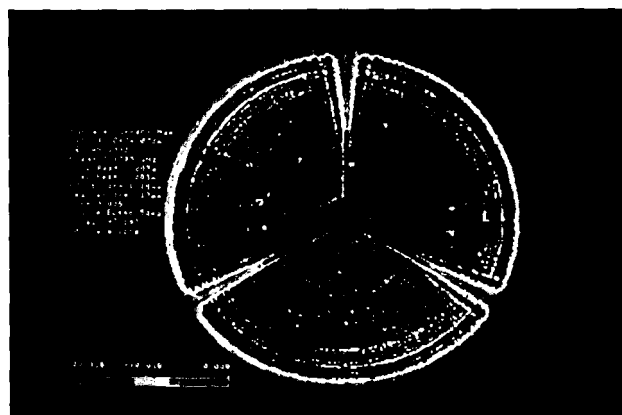

Figure 18: Derived Antenna Aperture Amplitude Map.

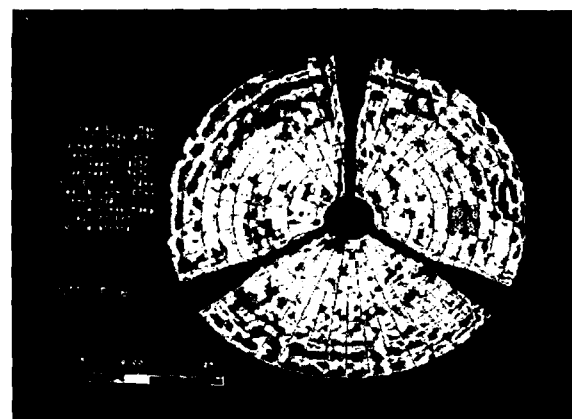Figure 19: DSS- 13 after Application of Panel Unbending

The comers of the panels, were observed to be pointing "up".

Applying four panel setting / unbending sessions at DSS-13 resulted in reduction of its surface rms error from 0.88 mm to 0.31 mm which improved its RF performance at Ka-band (32 GHz) by approximately 5 dB. The efficiency of the DSS- 13 measured from the BWG foeus (F3) is 57%. This corresponds to an estimated efficiency from the cassegrain F 1 focus of approximately 65%.

6. 34-M BWG Antenna Network

Between May of 1994 and December of 1996, three newly constructed NASA-JPL-DSN 34-M BWG antennas were measured holographically, and their panels and subreflectors were aligned. The three antennas are located in the Goldstone Deep Space Communication Complex (GDSCC) in California and are designated DSS-24, DSS-25, and DSS-26. The GDSCC is one of three DSN communication complexes. The other two are located near Madrid Spain (MDSCC), and Canberra Australia (CDSCC).

The panel setting for the three antennas were derived from measurements made from the cassegrain F 1 focus, utilizing Ku-band (11.7 GHz) beacon signal from the GSTAR-4 satellite observed at the nominal elevation angle of 47 degrees. Gravity and performance measurements at low elevation angles were using the
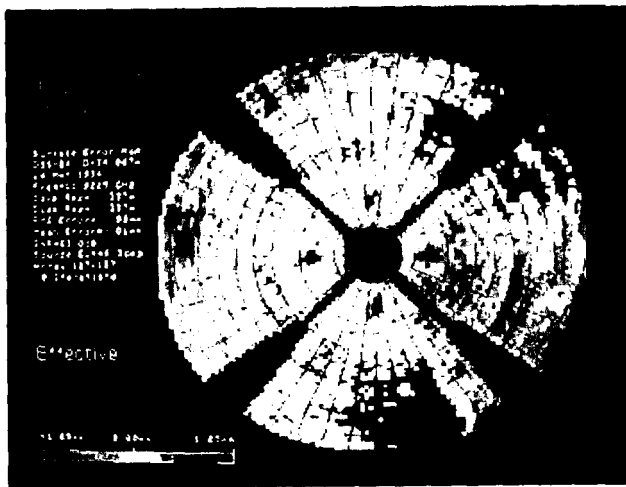
and in order to reduce time, the panel listing were rounded to the nearest ± I/8 of a screw turn. This enable resetting the entire dish in 8 hour period. The inferred (rss) panel setting accuracy is therefore 0.175 mm rms. The precision of the antenna surfaces in terms of Diameter / rms is 1.36x105 and the gain limit of the antennas occurs at 95 GHz. At 32 GHz (Ka-band), the averaged improved performance for each antenna due to panel setting is estimated to be 0.8 dB. This is equivalent to increasing the effective collecting area of each antenna by approximately 100 m^2 at Ka-band. The antenna rms surface error at 12.6 deg. elevation is 0.50 mm, and is mostly characterized by astigmatism due to gravity deformation as expected.

The accuracy of the high resolution maps in the above measurements is 0.07 mm to 0.10 mm rms, and the panel setting derivation accuracy is 0.025 mm to 0.0175 mm (25 to 17.5 micron) rms.
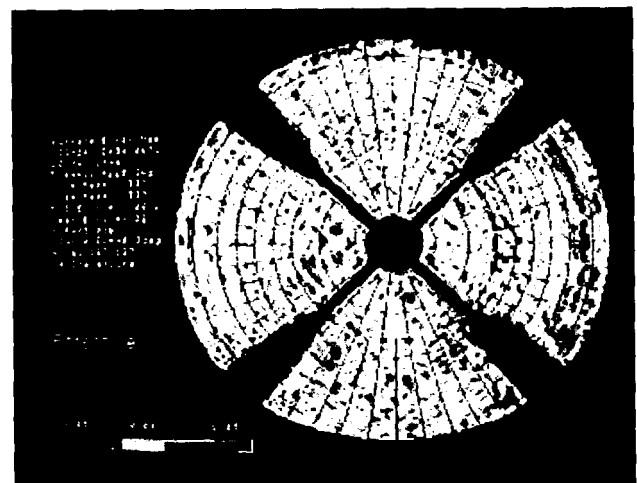

Figure 20: 11 SS-24 Surface after the Theodolite Setting

Figure 21: DSS-24 with a single Holography Application

beacon signal of the Intel sat-307 satellite observed at the nominal elevation angle of 12.7 degrees. At 47.0 degrees elevation, the normal rtns surface errors of the DS S-24, DSS-25, and DSS-26 as set by the theodolite were 0.50 mm, 0.50 mm, and 0.42 mm. respectively (Table 1). Figure 20 shows the holographically derived surface error map of DSS-24 after the alignment of the panels using the theodolite technique, achieving normal rms surface error of 0.50 mm.

After applying one session of the holographically derived panel setting, the normal rms surface error of each antenna was reduce to 0.25 mm, resulting in efficiencies of 75 .25% at X-band and 60.6% at Ka-band (measured from cassegrain focus at F 1 at 46.3 deg elevation, referenced to the input LNA). Figure 21. shows the holographically derived surface error map of DSS-24 after applying the holography derived panel setting, achieving a normal rms surface error of 0.25 mm. The 34-M BWG network antennas have 348 panels and 1716 adjusting screws. The rms surface of the individual panels is 0.127 mm and the rms surface error of the subreflector is 0.125 mm. Since a precision panel adjusting tool was not available

Subreflector Position Correction

The theory for the subreflector position correction via holography could be found in [11.]. The subreflector position correction is derived from the low order distortions in the antenna aperture phase function which is derived from low resolution (25x25 array for a 34-M antenna, or 5 1x51 for a 70-M antenna) holographic imaging. Two low resolution measurements are usually required due to the interaction of cubic and linear terms, the latter is due to systematic pointing errors. The time required for a single low resolution measurement is approximately 45 minutes and the data processing time is approximately 16 minutes. Figure 22 shows the far-field amplitude pattern of DSS-24 as found in the initial stage of the holographic measurements. Corrections to the subreflector controller X, Y, and Z axis were applied, 0.516 inches in the -X direction, 0.375 inches in the +Y direction and 0.135 inches in the +Z direction resulting in antenna far-field pattern shown in Figure 23. From observing the antenna far-field pattern in these images it is clear that the antenna went through a transformation from unfocused to focused. The performance improvement
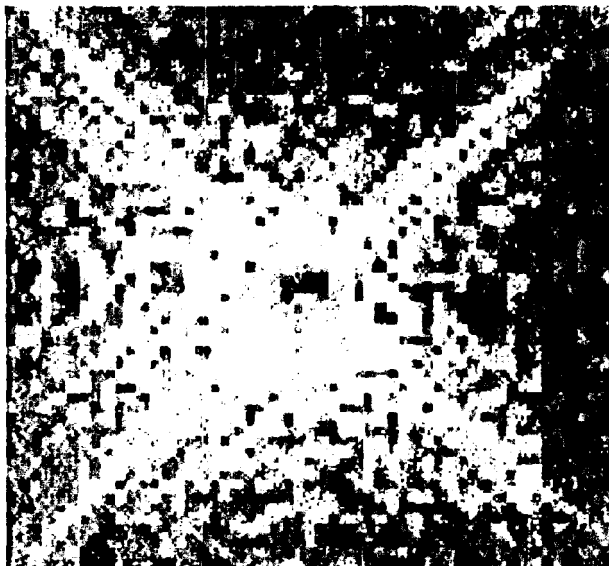
Figure 22: Antenna Far-Field Amplitude Pattern Before Subreflector position Corrections

Figure 23: Antenna Far-Field Amplitude Pattern After Subreflector position Corrections

obtained by setting the subreflector is 0.25 dB at X-band (8.45 GHz) and 3.6 dB at Ka-band (32 GHz). The derivation of the subreflector correction in the X-axis is especially critical since no servo drive controller (only manual mechanical adjustment are available) is available for this axis (for DSS-24), and therefore the traditional trial and error methods are not efficient. The corrections needed for the other 34-M BWG antennas were similar.

7. CONCL.US1ON

The microwave antenna holography has been effectively and reliably applied for significantly improved understanding and improved the microwave and mechanical performance of the large NASA/JPL DSN antenna and have provided new technology and science advances.

7. ACKNOWLEDGMENT

The author would like to acknowledge the support of the following individuals from JPL who contributed to the success of this program: Dan Bathker, Boris Seidel, Yahya Rahmat Samii, Carl Jones, Phil Withington and Herschel Jackson. Also the author would like to acknowledge Eikontech Ltd and Interferometrics Corp. for contributing to the success of this program.

REFERENCES

[1] D.J. Rochblatt and B.L. Seidel, "Microwave Antenna Holography", IEEE Trans. Microwave Theory and Techniques, Special Issue on Microwaves in Space. Vol. 40, NO. 6, pp.1 294-1300, June 1992
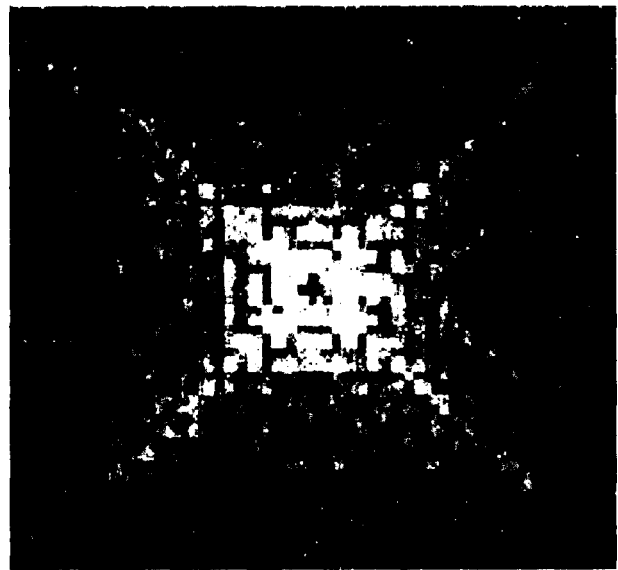
[2] P. H. Richter and D. J. Rochblatt, "A Microwave Performance Calibration System for NASA's Deep Space Network Antennas, Part 1: Assessment of Antenna Gain and Pointing, and Calibration of Radio Sources", Proceeding 10th Int.Conf. on Antennas and Propagation pp. 1.142- 1.149, vol. 1,14-17 April 1997.

[3] D. J. Rochblatt, P. H. Richter, and T. Y. Otoshi, "A Microwave Performance Calibration System for NASA's Deep Space Network Antennas, Part 2: Holography, Alignment, and Frequency Stability", Proceeding 10th Int.Conf. on Antennas and Propagation pp. 1.150-1.155, vol. 1, 14-17 April 1997.

[4] J.C. Bennet, A.P. Anderson, P.A. McInnes, and A.J.T. Whitaker, "Microwave Holographic Metrology of Large Reflector Antennas," IEEE Trans. Antennas Propagat., AP-24, pp. 295-303, 1976.

[5] M.P. Godwin, A.J.T. Whitaker, and A.P. Anderson, "Microwave Diagnostics of the Chilbolton 25 m Antenna Using OTS Satellite," in Proc. Inst. Elec. Eng. Int. Conf., York, England, 1981, pp. 232-236.

[6] P.F. Scott and M. Ryle, "A Rapid Method for Measuring the Figure of a Radio Telescope Reflector," Mon. Not. Roy. Astr. Sot., vol.178, pp. 539-545, 1977.

[7] D. J. Rochblatt, B. L. Seidel, "DSN Microwave Antenna Holography", JPL/TDA Progress Report 42-76, pp. 27-42, October - December 1983

[8] D. J. Rochblatt and Y. Rahmat-Samii, "Effects of Measurement Errors on Microwave Antenna Holography" IEEE Trans. Antennas Propagat., VOL. 39, NO. 7, pp. 933-942, July, 1991.

[9] Y. Rahmat-Samii, "Microwave Holography of Large Reflector Antennas--Simulation Algorithms," IEEE

Trans. Antennas Proagat., vol. AP-33, pp. 1 194-1203, 1985(see correct ions, IEEE Trans. Antennas Propagat., vol. AP-34, p. 853, 1986).

[10] C. E. Mayer, J.H. Davis, W.L. Peters, and W.J. Vogel, "A Holographic Surface Measurement of the Texas 4.9-meter Antenna at 86 GI 17," IEEE Trans. Instrum Meas., vol. IM-32, pp. 102-109, 1983.

[11] D. J. Rochblatt, P. M. Withington, and H. J. Jackson, "DSS-24 Microwave I Holography Measurements," publication of the Jet Propulsion laboratory, California Institute of Technology, JPL TDAPR No. 42-121, pp. 252-2? 70, May, 15 1995.

Table 1. Holography Historical Data

DSS*	Date	Meas. Freq. (GHz)	Resolution (meter)	Elevation (degrees)	Initial rms (mm)	Final rms (mm)	Gain Improvement (dB)		
							S-na	X-na	Ka-na
15	May 88	7.600	0.32	45.0	0.64	0.64	na	na	na
45	Jan 85	2.272	0.29	42.0	1.69	1.01	.10	1.39	20.1
45	Jul 88	7.260	0.32	42.0	1.01	0.53	0.03	().40	5.8
65	Nov 86	11.451	0.32	40.0	0.51	0.51	na	n a	na
14	Apr 88	12.198	0.42	47.0	1.26	0.64	0.05	0.64	9.3
43	Ott 87	12.750	0.44	47.0	1.18	0.65	0.04	0.59	8.5
43	Jun 88	12.750	0.44	47.0	0,68	0.64	0.00	0.06	0.8
63	Jul 87	11.451	0.42	42.0	1,58	0.65	0.09	1.17	16.9
13	Sep 90	12.198	0.32	46.0	0.88	0.43	0.02	0.32	4.6
13	Dcc91	12.198	0.32	46.0	0.50	0.50	na	na	na
13	Jan 92	12.198	0.32	46.0	0.68	0.37	0.01	0.18	2.5
13	Feb 94	12.198	0.32	46.0	0.38	0.31	0.00	0.03	0.32
24	May 94	11.922	0.33	46.3	0,50	0.25	.007	().1	1.27
14	Jan 95	11.712	0. 69	47.0	0.99	0.99	na	na	na
43	Sep 95	12.276	0. 80	46.2	0.97	0.97	na	na	na
63	Aug 95	12.502	1.61	43.3	1.10	1.10	na	na	na
25	Jun 96	11.913	0.33	47.0	0.50	0.25	.007	0.1	1.27
26	Oct 96	11.913	0.33	47.0	0.42	0.25	.()()4	().05	0.76

* DSS = Deep Space Sta)n (antenna's designation in ; DSN):
DSS- 14, 43, 63 are the 70-M antennas
DSS- 15, 45, 65 arc the 34-M HEF antennas
1) SS-24, 25, 26 are the 34-M BWG antennas
DSS- 13 is the 34-M R&D BWG antenna

David J. Rochblatt (S'81- M'82- SM'92) Received the B.S. Magna Cum Laude, and M.S. degrees in Electrical Engineering, both from the University of California 1 ,os Angeles (UCLA), in 1978 and 1980 respectively.

In 1981 Mr. Rochblatt joined the Jet Propulsion Laboratory California Institute of I'ethnology. Currently he is the manager of the Antenna Systems Work Area for the Telecommun icat ions and Mission Opcrat ions I'ethnology (TMOT) Program at J PL.
in 1995 Mr. Rochblatt received a NASA Exceptional Achievement Medal for the development and application of the microwave antenna holography system (MA I IST). He was a member of the imaging team that helped to characterize the flawed 1 lubble Space Telescope primary mirror using phase retrieval holography.

In the Antenna and Microwave Development Group he was a member of the team that designed the new NASA 70-meter antennas. As a group leader for the Tracking Systems and Applications Section he was responsible for the design of the front-end m icrowave subsystem for mobile Very long Baseline Interferometer (VLBI) station hardware. This included the design of dual-frequency Cassegrainian reflector antennas, and low-noise GaAs FET receiver amplifiers.
Mr Rochblatt served on the Scientific Advisory Committee of Save A 1 [cart Foundation, Cardiology Department of Cedar Sinai Medical Center and has been a consultant to several industrial and aerospace companies.

Mr. Rochblatt is a senior member of IEEE, a member of Tau Beta Pi and Eta Kappa Nu.